Angle-, Polarization-, and Wavelength-Resolved Light Scattering of Single Mie Resonators Using Fourier-Plane Spectroscopy

Hinamoto, Tatsuki
Hamada, Mikihiko
Sugimoto, Hiroshi
Fujii, Minoru

(Citation)
Advanced Optical Materials,9(8):2002192

(Issue Date)
2021-04-01

(Resource Type)
journal article

(Version)
Accepted Manuscript

Angle-, Polarization-, and Wavelength-Resolved Light Scattering of Single Mie Resonators Using Fourier-Plane Spectroscopy

Tatsuki Hinamoto, Mikihiko Hamada, Hiroshi Sugimoto, and Minoru Fujii**

Dr. T. Hinamoto, Mr. M. Hamada, Dr. H. Sugimoto, Prof. M. Fujii
Department of Electrical and Electronic Engineering, Graduate School of Engineering, Kobe University, Rokkodai, Nada, Kobe 657-8501, Japan
E-mail: tatsuki.hinamoto@gmail.com
E-mail: fujii@eedept.kobe-u.ac.jp

Dr. H. Sugimoto
JST-PRESTO, Honcho 4-1-8, Kawaguchi, Saitama 332-0012, Japan

Keywords: Mie resonance, back focal plane, multipolar interference, nanoantenna, directionality, Kerker condition

Interference between multipole modes of Mie resonance provides the possibility to tailor a radiation pattern of a sub-wavelength optical resonator. Unidirectional scattering arising from constructive and destructive interferences between electric and magnetic dipolar modes in a nanoantenna allows us to design a variety of metasurfaces. However, experimental determination of radiation patterns of an individual nanoobject and the decomposition into multipoles have not been performed under plane wave illumination due to the inability of angular analysis in a conventional optical microscope. To this end, we develop an angle-, polarization-, and wavelength-resolved microscopy setup to measure radiation patterns of an individual nanoobject. We employ a single spherical silicon nanosphere as an ideal Mie resonator and measure the angle- and polarization-resolved scattering in the angular range from 30 to 150° against the incident angle. We show that Mie scattering from the electric and magnetic dipoles of a single silicon nanosphere are selectively measured in the setup.

1. Introduction

A sub-wavelength optical resonator enables efficient manipulation of electromagnetic fields at the nanoscale and can be a building block of functional metamaterials and metasurfaces.[1–9] Recently, dielectric resonators made of high-refractive-index semiconductors are energetically studied due to the possession of high scattering efficiency and low-loss Mie resonances.[10] In

planar metasurface devices made from all-dielectric Mie resonators, the transmission efficiency reaches the value equivalent to that of a glass plate (>90%).[11,12]

The reported high transmission efficiency can be attributed to tailored scattering radiation patterns of individual building blocks enabled by multipolar interferences between electric and magnetic Mie resonances.[11,13] For example, unidirectional scattering occurs due to the interference between electric dipole (ED) and magnetic dipole (MD) resonances (known as the Kerker-type directionality), which improves the efficiency of transmission type metasurfaces by suppressing the reflection loss.[11,14,15] Various directional nanoantennas utilizing interferences between multiple resonances, for example, a dielectric or a metallodielectric dimer[16–21], a Yagi-Uda antenna[22], and more, are proposed.[23–25] Besides, transverse scattering, which means that a nanostructure scatters light neither to forward nor backward directions, but to in-plane, has been achieved by the interference between dipoles and off-resonant quadrupoles.[26] Furthermore, with a nanoantenna having an asymmetric radiation pattern, a metalens with a near-unity numerical aperture (>0.99) has been realized.[27]

To maximize the performance of metasurfaces, evaluation of the scattering pattern of individual nanoresonators is essential. Although it has been analyzed in detail by theoretical calculation or simulations, only primitive measurements have been performed in experiments due to some technical difficulties. Usually, a scattering spectrum of a single nanoobject is measured with an optical microscope in the dark-field geometry. Scattering to forward or backward directions is measured by illuminating light to a nano-object from the top or the bottom by dark-field condensers and collecting the scattered light directed within the numerical aperture (N.A.) of an objective.[15,28] Therefore, the term “forward and backward scattering” does not often mean scattering to 0° and 180° directions, respectively, but means “almost” forward and backward directions, respectively, *i.e.*, scattering to large angle ranges

are averaged. Another problem of the conventional dark-field configuration using grazing angle ring-shaped illumination is the smearing of the polarization information.

In this work, we develop a dark-field optical microscopy system, which is capable of angle-, polarization-, and wavelength-resolved scattering measurements over a wide angular range from 22° to 158° against the incident direction. This is enabled by combining specifically designed dark-field illumination and Fourier-plane (FP) imaging technique. FP imaging, in other words back focal plane imaging, is a technique that resolves information in a FP of a lens. In contrast to conventional imaging in an image-plane (IP), the FP has momentum information of light, and thus angular radiation patterns can be obtained. In the field of nanophotonics, it is often utilized to measure the radiation pattern of quantum emitters[29,30], cathodoluminescence (CL)[31–35], and lasing[36], and to visualize propagation of surface plasmon polaritons[37–39]. The technique has also been applied to directional light scattering by dielectric resonators[23,40]. However, angle- and polarization-resolved spectral measurements of a nano-object over a wide spectral and angular range have not been performed.

We employ a single spherical silicon nanoparticle as an ideal Mie resonator to evaluate the constructed setup. We show that theoretically predicted angle and polarization dependence of the scattering spectra can be reproduced in the setup. We also show that angle- and polarization-resolved scattering measurements allow us to separately detect ED and MD resonances. Although separate detection of ED and MD resonances of a nano-object is possible by an attenuated total reflection (ATR) configuration[41], by using specifically tailored vector beams[42–45], and by cathodoluminescence (CL)[32], the setup developed in this work provides more comprehensive information under plane wave irradiation without utilizing special configurations and optical components. The setup can be applied to a nano-object with any shape and can provide valuable information for the development of a nanoantenna and a metasurface.

2. Results and discussion

2.1. Angle and polarization-resolved Fourier-plane spectroscopy

In order to conduct the angle-, polarization-, and wavelength-resolved scattering measurement, we update the illumination and detection setups of a conventional optical microscope. Here, we start from a typical inverted microscope (Ti-U, Nikon) equipped with an epi-illumination dark-field objective (50×, N.A. = 0.80) on the bottom and an upper dark-field condenser as shown in **Figure 1**a and c. In the transmission mode (Figure 1a), white light from a halogen lamp is shone via the upper condenser at the incident angle θ_{inc} = 75°, while white light from another lamp house is shone via the lower objective in the reflection mode (Figure 1c) at θ_{inc} = 105°. Scattered light is then collected by the bottom objective and relayed to a spectrometer (iHR320, Horiba Jobin Yvon) coupled with a charge-coupled device (CCD; Symphony, Horiba Jobin Yvon). Although the inverted microscope is adopted here, the methodology developed in this work is general regardless of whether it is inverted or upright-type.

In a conventional setup, a dark-field condenser has a ring-shaped aperture and illuminates a sample from all azimuths, and thus the azimuth cannot be defined. In this work, we limit the azimuthal angle of illumination (ϕ_{inc}) by placing a pin-hole at the position of the pupil to fix an incident angle (Figure 1b,d). This enables us to define scattering polar (θ) and azimuthal (ϕ) angles uniquely with respect to the direction of the incidence. In both transmission and reflection modes, the width of the azimuth ($\Delta\phi_{inc}$) is limited to ≈ 20°. For polarization-resolved measurements, linear polarizers are inserted in the illumination paths.

Next, we construct the detection setup based on the FP spectroscopy. As shown in Figure 1e, the scattered light is collected by the bottom objective, forming an angular distribution image in the back focal plane (*i.e.*, Fourier-plane). The image is then transferred to the entrance slit of the spectrometer using relay lenses. During the relay, a pinhole is inserted in an image plane as a spatial filter. Since the illumination plane and the orientation

of the spectrometer slit are parallelly aligned with each other, the slit resolves the scattered light in the azimuth. Therefore, the scattering intensity image on a CCD has the information in θ direction in addition to the wavelength along the vertical and horizontal axes, respectively. For a better illustration of the FP spectroscopy setup, FP images of a diffuse reflection standard are shown on the bottom panel of Figure 1e. When the 0th order diffraction is projected to the CCD without closing the slit, the FP image contains angular information in θ and ϕ. The FP image is then restricted in azimuth by the slit and spectrally dispersed by a grating, resulting in a two-dimensional (2D) scattering map of θ and wavelength. Note that the vertical axis of the raw data is proportional to $\sin\theta$, and it is transformed into θ with the arcsine function. The calibration of the θ value is made by measuring the reflection of a grating with a known groove density.

The angular range which can be obtained by designing the illumination and detection geometries is schematically summarized in Figure 1f-h. Given that N.A. = 0.8 corresponds to 53°, the objective collects scattered light from 22° to 128° and from 52° to 158° against the incident axis in the transmission and reflection modes, respectively. Thus, the angular range θ = 22° – 158° (136° in total) can be measured with an overlapping range of θ = 52° – 128° (Figure 1h). Slight increase of the range may be possible if a larger N.A. objective is used. However, since the largest collection angle is restricted by the incident angle of the upper dark-field condenser (θ_{inc} = 75°), drastic increase of the range is not possible.

2.2. Angle-resolved FP spectroscopy of silicon nanosphere

To evaluate the potential of the FP spectroscopy setup, we apply it for a crystalline silicon nanosphere shown in **Figure 2**. Since the sphericity and the crystallinity are very high as can be seen in Figure 2a and b, they can be regarded as an ideal Mie resonator. For the angle-resolved FP spectroscopy, a nanosphere is placed onto an optically thin (≈ 10 nm) silicon dioxide (SiO_2) support film (Figure 2c), enabling us to evaluate optical properties in

the simplest configuration without substrate-induced disturbance.[46] The scattering spectrum measured in a conventional setup for a Si nanosphere in Figure 2d is shown in Figure 2e. The nanosphere exhibits typical spectral response of Mie resonance, that is, ED (~ 540 nm) and MD (~ 660 nm) resonances. The spectrum is in good agreement with that of the simulation for a silicon nanosphere 168 nm in diameter (Figure 2f). The result of multipole decomposition is shown in Figure S1 (see Supporting Information).[47] We utilize the same nanosphere (Figure 2d) for the angle- and polarization-resolved measurements.

Before proceeding to angle-resolved spectroscopy of a nanosphere, we analyze the expected results by simulation. A simulated 2D map of angle-resolved scattering spectra for a silicon nanosphere 168 nm in diameter is shown in **Figure 3**a. In addition to strong scattering peaks of ED and MD Mie resonances around 550 and 660 nm, respectively, a weak peak arises at the shorter wavelength side of the ED resonance. The peak is assigned to the magnetic quadrupole (MQ) resonance. These modes exhibit different angular dependence. For example, the scattering intensity around the MD mode is almost twice larger in the forward direction ($\theta = 0°$) than the backward one ($\theta = 180°$), while that around the ED mode, the intensities are almost the same in both directions. This difference arises from the *so-called* Kerker condition; forward (backward) scattering is constructively enhanced in longer (shorter) wavelength side of the MD mode, where the first (second) Kerker condition is satisfied.[15,24,48]

Experimentally measured 2D map for the silicon nanosphere is shown in Figure 3b and c for transmission (22° to 128°) and reflection (52° to 158°) modes, respectively. We see that the observed angular and spectral features show overall agreement with the simulation in the angular range from $\theta \approx 30°$ to 150°. For example, around 30°, both ED and MD resonances are observed (Figure 3b) and in the 30-110° range, MD scattering is stronger than the ED one (Figure 3b and c). In the measured 2D map, the slight undulation of the intensity is seen in the vertical direction. This may be caused by undesirable filtering of certain angular

components by the relay lenses or the aperture. Nonetheless, the important features of Mie resonators such as the unidirectional behavior are well captured in the measurement.

Our FP spectroscopy setup allows us to extract a scattering spectrum at an arbitrary angle. As a benchmark, we extract θ = 50° and 130°scattering spectra from Figure 3, which corresponds to the geometry shown in **Figure 4**a. Figure 4b shows simulated scattering spectra at θ = 50° and 130°. The corresponding measured spectra are shown in Figure 4c. The measured and simulated spectra agree very well in both directions. Prominent ED and MD peaks are observed at θ = 50°, while both are broadened at 130°. Figure 4d and e show the ratio of the θ = 50° scattering spectrum to the 130° one obtained from the simulated and measured scattering spectra, respectively. The spectral shape again agrees very well. The ratio reaches around 14 at 709 nm in the measured spectrum, where the backward scattering is strongly suppressed.

The FP spectroscopy setup is also capable of analyzing a radiation pattern at an arbitrary wavelength. In Figure 4f, a simulated radiation pattern at the peak wavelength of the intensity ratio spectrum in Figure 4d (≈ 710 nm) is shown. Light is predominantly radiated in the forward direction ($0 < \theta < 90°$), and the backward scattering ($\theta > 90°$) is strongly suppressed at the wavelength due to the Kerker-type interference. Likewise, the corresponding measured radiation pattern shown in Figure 4g shows the same directionality, that is, the backward scattering ($\theta > 90°$) is steeply suppressed.

2.3. Angle- and polarization-resolved FP spectroscopy

Under illumination by s- and p-polarized light, orientations of ED and MD moments are fixed to a certain orientation. This enables us to selectively detect ED and MD moments by angle-resolved FP spectroscopy. In the framework of Mie theory,[49] multipolar contributions can be expressed using Mie coefficients a_n and b_n which correspond to nth order electric and magnetic resonances, respectively. Following the definition of θ and ϕ in

references[50,51], the polarization-dependent far-field scattering intensities I_{sca}^{θ} and I_{sca}^{ϕ} by a sphere in free space are given by

$$I_{sca}^{\theta} = |E_{s\theta}|^2 \propto \left| \frac{cos\,\phi}{-ik} \sum_{n=1}^{\infty} E_n (a_n \tau_n(cos\theta) + b_n \pi_n(cos\theta)) \right|^2$$
$$I_{sca}^{\phi} = \left|E_{s\phi}\right|^2 \propto \left| \frac{sin\,\phi}{ik} \sum_{n=1}^{\infty} E_n \left(a_n \pi_n(cos\theta) + b_n \tau_n(cos\theta)\right) \right|^2 \quad (1)$$

, where $E_{s\theta}$ and $E_{s\phi}$ denote the scattered electric fields, k is a free space wavenumber, $E_n = (2n+1)/n(n+1)$, π_n and τ_n are the angle-dependent functions.[50] Given our experimental setup which is capable of defining ϕ by the entrance slit, setting ϕ to 90° and 0° corresponds to the detection of s- and p-polarized light, respectively (**Figure 5**). Therefore, only I_{sca}^{ϕ} is detected under s-polarized light illumination, while I_{sca}^{θ} is the matter for p-polarization. In this condition, θ-dependent angular distribution for each polarization can be simply illustrated as shown in Figure 5. As indicated in the figure, ED and MD contributions can be separated by further imposing a restriction of θ = 90°, which leads to $\pi_1 = 1$ and $\tau_1 = 0$ and $I_{\mathrm{sca}}^{s} \propto \left|\frac{1}{-ik} E_1(a_1)\right|^2$ and $I_{\mathrm{sca}}^{p} \propto \left|\frac{1}{ik} E_1(b_1)\right|^2$ under the dipolar approximation. Note that this strategy can be applied also to the second-order ($n = 2$) terms. For the quadrupolar contributions, $I_{\mathrm{sca}}^{s} \propto \left|\frac{1}{-ik} E_2(-3b_2)\right|^2$ and $I_{\mathrm{sca}}^{p} \propto \left|\frac{1}{ik} E_1(-3a_2)\right|^2$ at $\theta = 90°$.[51]

In **Figure 6**a and b, simulated 2D maps of angle-resolved scattering spectra under s- and p-polarized illuminations, respectively, are shown. In the simulated data, when θ is around 90°, ED and MD modes are separately observed in s- and p-polarized illuminations, respectively. This behavior is reproduced in the measured spectra in Figure 6c-f, although the data are noisy. In Figure 6c-f, the quality of the data is better in the reflection mode (Figure 6e,f) than in the transmission mode (Figure 6c, d). This may be due to better alignment of the

optical setup in the reflection mode because of the usage of the same objective for illumination and detection.

To better visualize the selective detection of ED and MD scattering, simulated scattering spectra at $\theta = 90°$ are extracted from Figure 6a and b. **Figure 7**a shows the results. ED and MD scattering is selectively detected in the s- and p-polarized illuminations. This can be confirmed by comparing the spectra with analytically decomposed spectra in the supporting information (Figure S1). The corresponding measured spectra taken from Figure 6e and f are shown in Figure 7b. We can see obvious agreement between the simulations and measurements both in the s- and p-polarized illumination. Therefore, the ED and MD contributions to the scattering spectrum of an individual sub-wavelength resonator can be separately obtained in the angle-, polarization-resolved FP spectroscopy setup.

Finally, we would like to clarify the limitation of the developed setup. The first one is the fixed illumination direction. For the measurement of an anisotropic object in a specific illumination direction, the sample needs to be tilted. The second one is the limited range of θ. In the dark-field configuration used in this work, measurement of the full $0° \leq \theta \leq 180°$ range is not possible, and it is limited to the 22 – 158° range in the present work. Nonetheless, the capability to measure angle-, polarization- and spectrally resolved scattering spectra of a single nanoobject under incoherent plane wave illumination is unique and can provide a new tool for the development of nanoantennas.

3. Conclusion

We have developed a Fourier-plane spectroscopy setup to measure angle- and polarization-resolved scattering spectra of a single Mie resonator by implementing facile modification on a conventional dark-field optical microscope and spectroscopy equipment. By using a spherical silicon nanoparticle as a benchmark, we analyzed spectrally resolved radiation patterns of a single subwavelength Mie resonator. We also developed the

methodology to selectively detect the electric and magnetic dipole contributions in the scattering spectra. Since the developed process does not require any special equipment, configurations, and optical components, it may be utilized for optical characterization of a variety of nanoantennas.

4. Experimental Methods

Preparation of silicon nanospheres: Silicon nanospheres were synthesized with a recently developed method, which is based on phase separation of silicon-rich borophosphosilicate glass at T_a = 1500 °C and subsequent etching by a hydrofluoric acid solution.[52,53] The synthesized nanospheres were dispersed in ethanol and then drop-cast on a TEM grid covered with a 10 nm thick SiO_2 film.

Simulation: Simulated scattering properties were obtained with the finite-difference time-domain (FDTD) method (FDTD Solutions, Lumerical Inc.). The simulation model consists of a silicon nanosphere in air and a plane wave source based on a total-field scattered-field (TFSF) technique surrounded by perfectly matched layer (PML) boundaries. The refractive index of silicon was taken from literature.[54] Substrates were not considered. The angular scattering spectra were obtained from the far-field scattered power after far-field projection. The scattering spectrum in the conventional setup was simulated by integrating the power over the light cone defined by the numerical aperture and the illumination angle of the objective.

Supporting Information

Supporting Information is available from the Wiley Online Library or from the author.

Acknowledgements

T. H. acknowledges the support under Grant-in-Aid for JSPS Research Fellows. H.S. acknowledges the support provided by JST, PRESTO Grant Number JPMJPR19T4. This work was partly supported by JSPS KAKENHI Grants 18J20276 and 18KK0141.

Received: ((will be filled in by the editorial staff))
Revised: ((will be filled in by the editorial staff))
Published online: ((will be filled in by the editorial staff))

References

[1] J. Rho, *MRS Bull.* **2020**, *45*, 180.

[2] R. Paniagua-Dominguez, S. T. Ha, A. I. Kuznetsov, *Proc. IEEE* **2020**, *108*, 749.

[3] C. U. Hail, A. U. Michel, D. Poulikakos, H. Eghlidi, *Adv. Opt. Mater.* **2019**, *7*, 1801786.

[4] R. Paniagua-Domínguez, B. Luk'yanchuk, A. Miroshnichenko, J. A. Sánchez-Gil, *J. Appl. Phys.* **2019**, *126*, 150401.

[5] A. Vaskin, R. Kolkowski, A. F. Koenderink, I. Staude, *Nanophotonics* **2019**, *8*, 1151.

[6] R. Won, *Nat. Photonics* **2019**, *13*, 585.

[7] I. Staude, T. Pertsch, Y. S. Kivshar, *ACS Photonics* **2019**, *6*, 802.

[8] M. Taghinejad, W. Cai, *ACS Photonics* **2019**, *6*, 1082.

[9] H. Hasebe, H. Sugimoto, T. Hinamoto, M. Fujii, *Adv. Opt. Mater.* **2020**, 2001148.

[10] A. I. Kuznetsov, A. E. Miroshnichenko, M. L. Brongersma, Y. S. Kivshar, B. Luk'yanchuk, *Science* **2016**, *354*, aag2472.

[11] M. Decker, I. Staude, M. Falkner, J. Dominguez, D. N. Neshev, I. Brener, T. Pertsch, Y. S. Kivshar, *Adv. Opt. Mater.* **2015**, *3*, 813.

[12] S. Kruk, Y. Kivshar, *ACS Photonics* **2017**, *4*, 2638.

[13] E. Poutrina, A. Urbas, *J. Opt.* **2014**, *16*, 114005.

[14] L. Wang, S. Kruk, H. Tang, T. Li, I. Kravchenko, D. N. Neshev, Y. S. Kivshar, *Optica* **2016**, *3*, 1504.

[15] Y. H. Fu, A. I. Kuznetsov, A. E. Miroshnichenko, Y. F. Yu, B. Luk'yanchuk, *Nat. Commun.* **2013**, *4*, 1527.

[16] R. Guo, E. Rusak, I. Staude, J. Dominguez, M. Decker, C. Rockstuhl, I. Brener, D. N. Neshev, Y. S. Kivshar, *ACS Photonics* **2016**, *3*, 349.

[17] A. Devilez, B. Stout, N. Bonod, *ACS Nano* **2010**, *4*, 3390.

[18] J. Ho, Y. H. Fu, Z. Dong, R. Paniagua-Dominguez, E. H. H. Koay, Y. F. Yu, V. Valuckas, A. I. Kuznetsov, J. K. W. Yang, *ACS Nano* **2018**, *12*, 8616.

[19] P. Albella, T. Shibanuma, S. A. Maier, *Sci. Rep.* **2015**, *5*, 1.

[20] T. Shibanuma, T. Matsui, T. Roschuk, J. Wojcik, P. Mascher, P. Albella, S. A. Maier, *ACS Photonics* **2017**, *4*, 489.

[21] T. Shibanuma, P. Albella, S. A. Maier, *Nanoscale* **2016**, *8*, 14184.

[22] W. Liu, A. E. Miroshnichenko, D. N. Neshev, Y. S. Kivshar, *ACS Nano* **2012**, *6*, 5489.

[23] J. Li, N. Verellen, D. Vercruysse, T. Bearda, L. Lagae, P. Van Dorpe, *Nano Lett.* **2016**, *16*, 4396.

[24] C. Ma, J. Yan, Y. Huang, G. Yang, *Adv. Opt. Mater.* **2017**, *5*, 1700761.

[25] Y. Tsuchimoto, T. Yano, T. Hayashi, M. Hara, *Opt. Express* **2016**, *24*, 14451.

[26] H. K. Shamkhi, K. V. Baryshnikova, A. Sayanskiy, P. Kapitanova, P. D. Terekhov, P. Belov, A. Karabchevsky, A. B. Evlyukhin, Y. Kivshar, A. S. Shalin, *Phys. Rev. Lett.* **2019**, *122*, 193905.

[27] R. Paniagua-Domínguez, Y. F. Yu, E. Khaidarov, S. Choi, V. Leong, R. M. Bakker, X. Liang, Y. H. Fu, V. Valuckas, L. A. Krivitsky, A. I. Kuznetsov, *Nano Lett.* **2018**, *18*, 2124.

[28] N. Li, Y. Lai, S. H. Lam, H. Bai, L. Shao, J. Wang, *Adv. Opt. Mater.* **2020**, *2001081*, 2001081.

[29] A. G. Curto, G. Volpe, T. H. Taminiau, M. P. Kreuzer, R. Quidant, N. F. van Hulst, *Science* **2010**, *329*, 930.

[30] T. Bucher, A. Vaskin, R. Mupparapu, F. J. F. Löchner, A. George, K. E. Chong, S. Fasold, C. Neumann, D.-Y. Choi, F. Eilenberger, F. Setzpfandt, Y. S. Kivshar, T. Pertsch, A. Turchanin, I. Staude, *ACS Photonics* **2019**, *6*, 1002.

[31] T. Sannomiya, A. Konečná, T. Matsukata, Z. Thollar, T. Okamoto, F. J. García de Abajo, N. Yamamoto, *Nano Lett.* **2020**, *20*, 592.

[32] T. Matsukata, N. Matthaiakakis, T. Yano, M. Hada, T. Tanaka, N. Yamamoto, T. Sannomiya, *ACS Photonics* **2019**, *6*, 2320.

[33] T. Coenen, E. J. R. Vesseur, A. Polman, A. F. Koenderink, *Nano Lett.* **2011**, *11*, 3779.

[34] C. Colliex, M. Kociak, O. Stéphan, *Ultramicroscopy* **2016**, *162*, A1.

[35] P. Shekhar, M. Malac, V. Gaind, N. Dalili, A. Meldrum, Z. Jacob, *ACS Photonics* **2017**, *4*, 1009.

[36] S. T. Ha, Y. H. Fu, N. K. Emani, Z. Pan, R. M. Bakker, R. Paniagua-Domínguez, A. I. Kuznetsov, *Nat. Nanotechnol.* **2018**, *13*, 1042.

[37] A. Drezet, A. Hohenau, D. Koller, A. Stepanov, H. Ditlbacher, B. Steinberger, F. R. Aussenegg, A. Leitner, J. R. Krenn, *Mater. Sci. Eng. B Solid-State Mater. Adv. Technol.* **2008**, *149*, 220.

[38] A. Hohenau, J. R. Krenn, A. Drezet, O. Mollet, S. Huant, C. Genet, B. Stein, T. W. Ebbesen, *Opt. Express* **2011**, *19*, 25749.

[39] P. E. Landreman, M. L. Brongersma, *Nano Lett.* **2014**, *14*, 429.

[40] T. Kosako, Y. Kadoya, H. F. Hofmann, *Nat. Photonics* **2010**, *4*, 312.

[41] J. Xiang, J. Li, Z. Zhou, S. Jiang, J. Chen, Q. Dai, S. Tie, S. Lan, X. Wang, *Laser Photon. Rev.* **2018**, *12*, 1800032.

[42] U. Manna, H. Sugimoto, D. Eggena, B. Coe, R. Wang, M. Biswas, M. Fujii, *J. Appl. Phys.* **2020**, *127*, 033101.

[43] P. Woźniak, P. Banzer, G. Leuchs, *Laser Photon. Rev.* **2015**, *9*, 231.

[44] J. A. Parker, H. Sugimoto, B. Coe, D. Eggena, M. Fujii, N. F. Scherer, S. K. Gray, U. Manna, *Phys. Rev. Lett.* **2020**, *124*, 097402.

[45] J. Mun, S.-W. Moon, J. Rho, *Opt. Express* **2020**, *28*, 36756.

[46] H. Sugimoto, T. Hinamoto, M. Fujii, *Adv. Opt. Mater.* **2019**, *1900591*, 1900591.

[47] T. Hinamoto, M. Fujii, **2020**.

[48] M. Kerker, D.-S. Wang, C. L. Giles, *J. Opt. Soc. Am.* **1983**, *73*, 765.

[49] G. Mie, *Ann. Phys.* **1908**, *330*, 377.

[50] C. F. Bohren, D. R. Huffman, Eds. , *Absorption and Scattering of Light by Small Particles*, Wiley-VCH Verlag GmbH, Weinheim, Germany, **1998**.

[51] T. Hinamoto, S. Hotta, H. Sugimoto, M. Fujii, *Nano Lett.* **2020**, *20*, 7737.

[52] H. Sugimoto, M. Fujii, *Adv. Opt. Mater.* **2017**, *5*, 1700332.

[53] H. Sugimoto, T. Okazaki, M. Fujii, *Adv. Opt. Mater.* **2020**, *2000033*, 2000033.

[54] Edward D. Palik, *Handbook of Optical Constants of Solids*, Academic Press, San Diego, USA, **1998**.

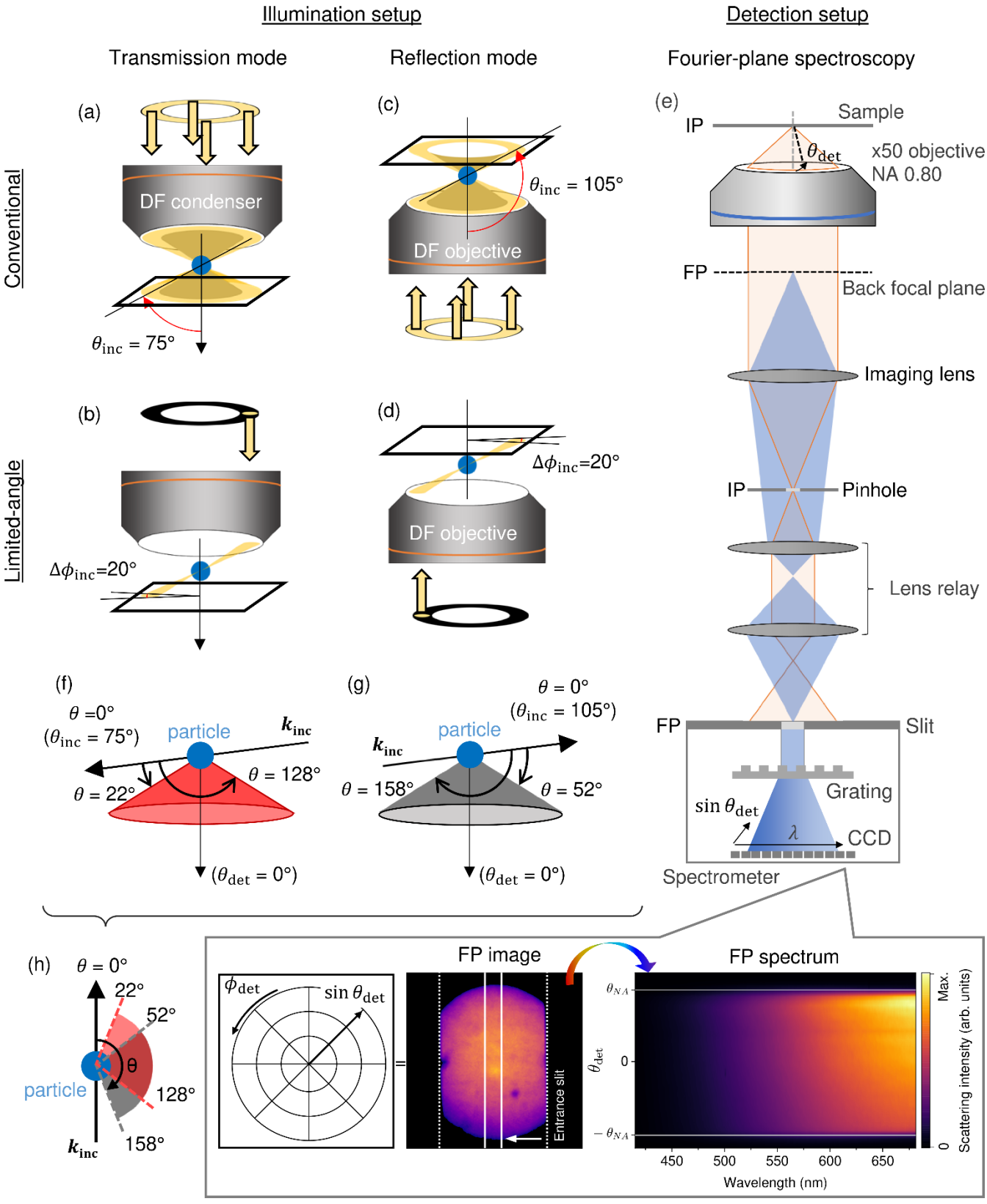

Figure 1. Schematics of measurement configurations. (a-d) Illumination setups in (a,b) transmission- and (c,d) reflection modes. (a,c) and (b,d) are conventional ring-shape and limited azimuthal angle (ϕ_{inc}) illumination, respectively. (e) Detection setup using Fourier-plane spectroscopy. (f,g) Detectable angle range in (f) transmission and (g) reflection modes. (h) Total detection angle range against the illumination direction (θ = 0°).

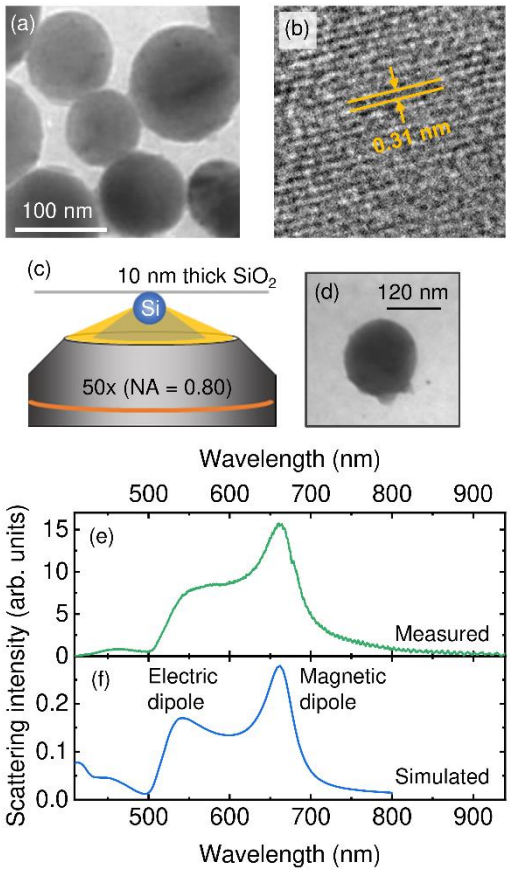

Figure 2. Crystalline silicon nanospheres as ideal Mie resonators. (a) TEM and (b) high-resolution TEM images of the synthesized nanospheres. (c-e) Optical spectroscopy of the silicon nanosphere in the conventional dark-field configuration. (c) Illustration of the measurement setup. (d) TEM image of the nanosphere measured in this work. (e) Scattering spectrum measured using a conventional setup. (f) Simulated scattering spectrum in which the setup is considered.

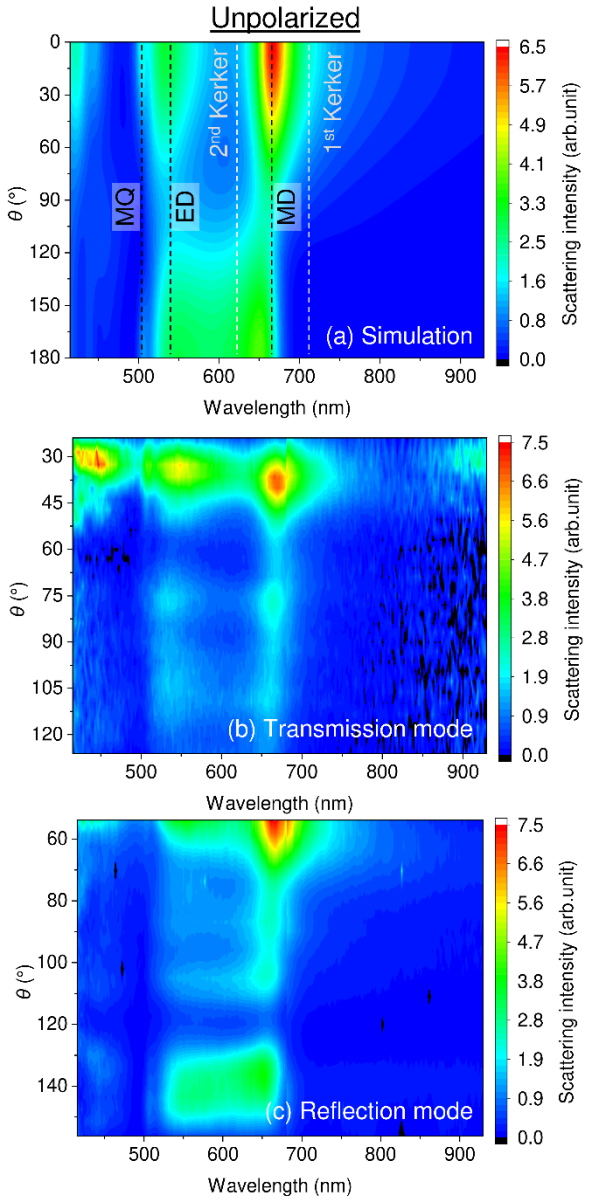

Figure 3. (a) Simulated and (b,c) measured angular-scattering intensities under unpolarized-light illumination as a function of wavelength and scattered angle (θ). b and c are measured in transmission and reflection modes, respectively.

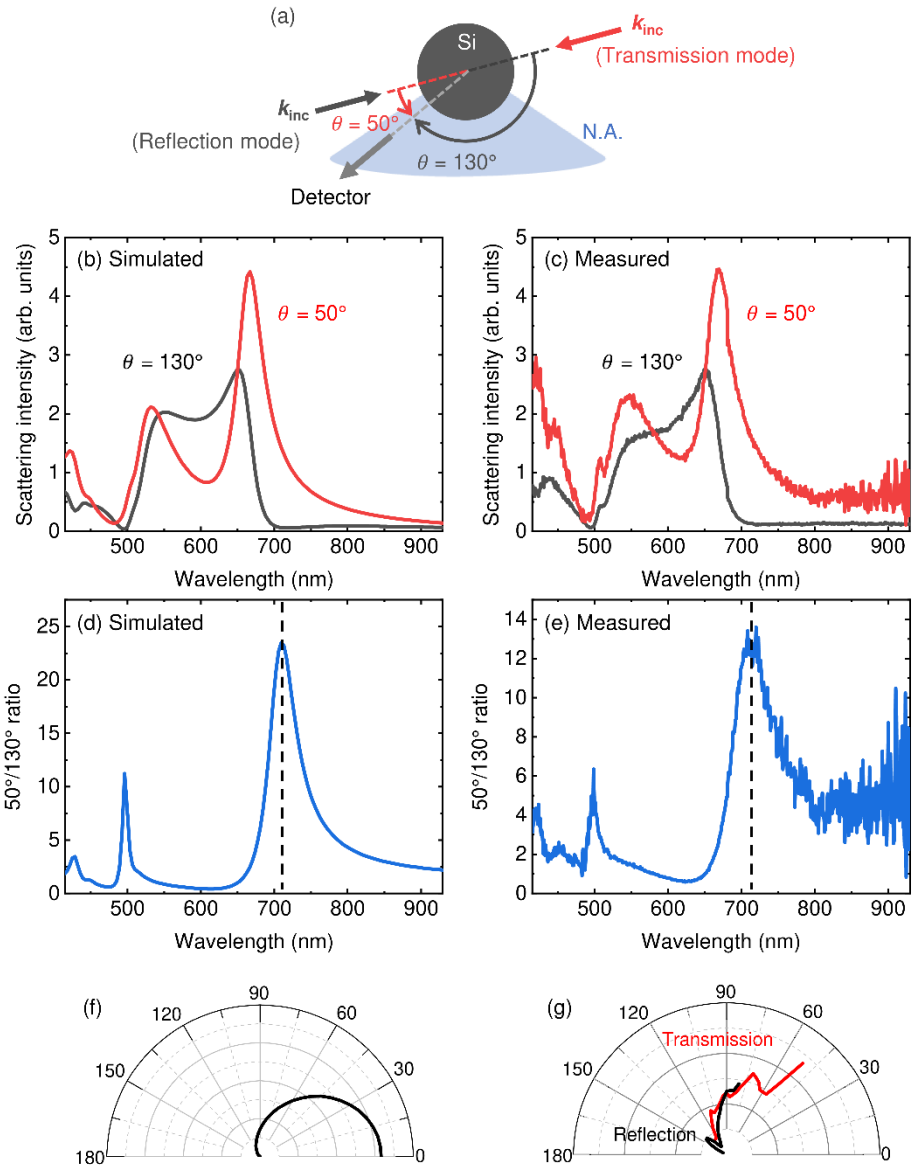

Figure 4. Evaluation of the directionality under unpolarized-light illumination. (a) Measurement geometry. (b,d,f) Simulated data and (c,e,g) measured data. (b,c) Scattering spectra at θ = 50° (red curve) and θ = 130° (black curve), (d,e) Ratio of the θ = 50° scattering spectrum to the θ = 130° one, and (f,g) θ-dependent radiation patterns at the peak wavelength of d and e (~715 nm).

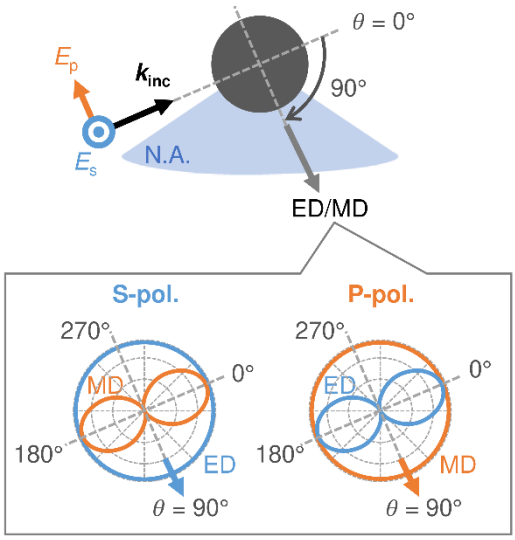

Figure 5. Schematic illustration of selective detection of ED and MD Mie resonances with the angle- and polarization-resolved FP spectroscopy.

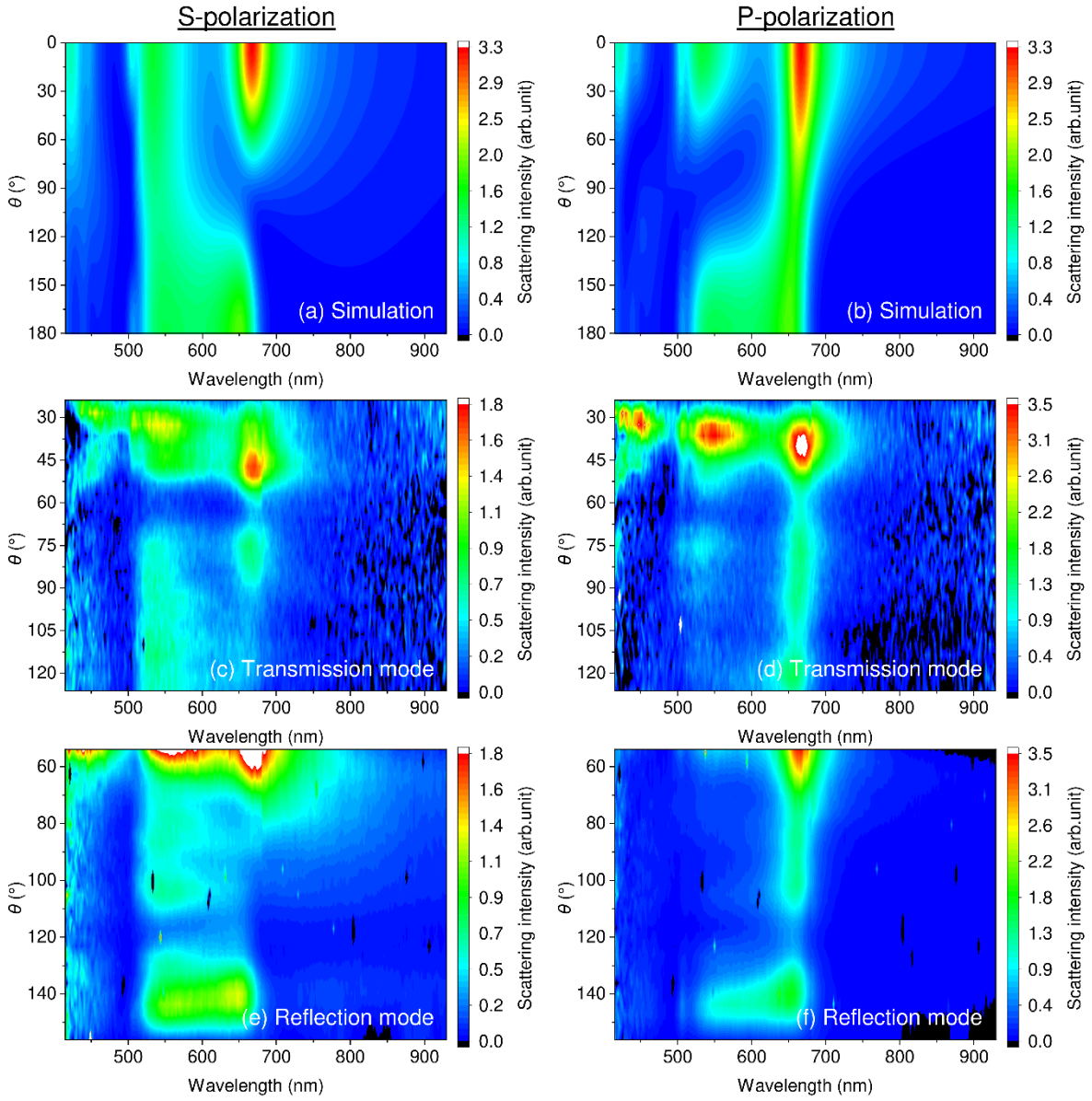

Figure 6. (a,b) Simulated and (c-f) measured angular-scattering intensities under (a,c,e) s- and (b,d,f) p-polarized illumination. The ordinate is the scattered angle (θ), and the abscissa is the wavelength. c,d and e,f are obtained in the transmission and reflection modes, respectively.

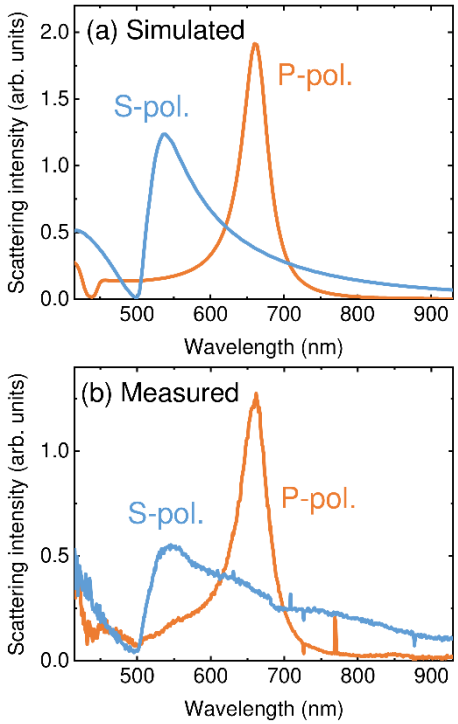

Figure 7. (a) Simulated and (b) measured scattering spectra under s- and p-polarized illumination. The data are obtained from Figure 6 at $\theta = 90°$.

In combination with tailored dark-field illumination and Fourier plane spectroscopy, angle-resolved scattering measurement of individual nanoobjects is presented. By employing a silicon nanosphere as an ideal scatterer, we demonstrate an analysis of directional scattering arising from the interference of Mie resonances. Moreover, by further resolving in polarization, the developed method enables us to separately measure electric and magnetic dipolar scatterings.

T. Hinamoto,* M Hamada, H Sugimoto, and M Fujii*

Angle-, Polarization-, and Wavelength-Resolved Light Scattering of Single Mie Resonators Using Fourier-Plane Spectroscopy

ToC figure